Rainfall Monitoring Based on Machine Learning by Earth-Space Link in the Ku Band

Minghao Xian, Xichuan Liu, Min Yin, Kun Song, Shijun Zhao, and Taichang Gao

***Abstract*—Recently, the oblique earth-space links (OELs) between satellite and earth station have been used for rainfall monitoring as a supplement to existing observation methods. Most recent studies achieved the rainfall measurement by OELs based on the empirical method such as power-law (PL) model. In practice, two crucial issues need to be addressed: 1) identification of rain and no-rain periods; and 2) determination of attenuation baseline. To solve these problems, this article adopts several machine learning algorithms based on the analysis of earth-space link signal characteristics. For the first issue, we choose the support vector machine as a classifier and the adaptive synthetic sampling algorithm is deployed to eliminate the effects caused by the data imbalance. For the second issue, the long short-term neural network is selected for the determination of attenuation baseline since it has a good ability to solve time-series problem. In terms of the rainfall inversion, we establish a new model by combining the back-propagation (BP) network and genetic algorithm (GA). The PL model is also used as a comparison. To validate the proposed method, we set up an earth-space link that receives the signal from AsiaSat5 in 12.32 GHz. The results demonstrate that the two issues are successfully addressed and the inversion of precipitation is also carried out. Compared to disdrometer, the correlation and mean absolute error of GA-BP model are 0.83 and 1.30 mm/h, respectively, indicating a great potential to use densely OELs for global precipitation monitoring.**

***Index Terms*—Earth-space link, ku-band, machine learning, rainfall monitoring, remote sensing.**

I. Introduction

ACCURATE and real-time rainfall measurement plays an important role in many aspects of human life such as agricultural issues, water resource management, and natural disaster warning. Existing rainfall detection method mainly comprises rain gauge, weather radar, and weather satellite [1]. Based on the exploitation of existing radio spectrum sources, the opportunistic use of microwave links has become a new approach to detect precipitation. Messer *et al.* first suggested the application of commercial wireless communication networks to environmental monitoring [2]. In recent years, the use of horizontal microwave links (HMLs) has been developed rapidly in many fields such as path-average rain intensity inversion [3], [4], radar calibration [5], and regional rainfall monitoring [6]. With the deployment of 5G wireless system, there will be more and more millimeter-wave HMLs all over the world. Relevant research has shown these densely distributed HMLs are capable of monitoring precipitation in urban areas [7]. It can be said HMLs have become a supplement to existing rainfall measurement method.

In fact, the oblique earth-space links (OELs) as another source of microwave links also have potential to measure precipitation. Barthes *et al.* used the OELs from television satellite located at geostationary earth orbit (GEO) and successfully retrieved the rain intensity in Paris area [8]. In space, there are hundreds of GEO satellites operated by broadcast and telecommunication companies, and satellites emit stable microwave signal in C (4–8 GHz) and Ku (12–18 GHz) bands toward the earth. Theoretically speaking, three GEO satellites are capable of covering the whole globe expect polar regions, and with sufficient OELs, it is possible to monitor the global precipitation. Mercier *et al.* proved the feasibility of this idea through their experiment [9]. They made use of four OELs to successfully retrieve 2-D rain maps with high resolution in Vivarais region in the south of France. Now there are many research works demonstrating that the GEO OELs are qualified for real-time rainfall monitoring [10]–[13].

Recently, communication satellite constellation (CSC) has been under construction by many technology companies such as spaceX and OneWeb [14], [15]. The CSC consists of many low-earth orbit (LEO) satellites using Ku, Ka (27–40 GHz), or even higher bands. For example, OneWeb plans to adopt 882 LEO satellites in the Ku band to establish their first-generation CSC and provides commercial services for global users in 2021 [15]. The Ku and Ka bands satisfy the demand of high capability and available bandwidth, at the same time, they are very suitable for rainfall measurement. Moreover, to make the CSC commercially feasible, user ground terminals must be at a lower price. The relevant studies have shown the potential of LEO OEL system for precipitation monitoring [16], [17]. Therefore, in the near future, using the densely commercial OEL networks can develop a high-resolution precipitation observation system all over the world, which is part of the wireless environmental sensor networks [18].

Different from HML, there are more complex factors affecting the OEL because it penetrates the whole troposphere. Due to the effects of no-rain atmospheric factors such as gasses, cloud, and turbulence [12], [13], two critical issues need to be addressed

Manuscript received April 10, 2020; revised June 7, 2020 and June 18, 2020; accepted June 19, 2020. Date of publication June 23, 2020; date of current version July 6, 2020. This work was supported in part by the National Natural Science Foundation of China under Grant 41975030, Grant 41505135, and Grant 41475020, and in part by the National Natural Science Foundation of Jiangsu Province under Grant BK20181337. *(Corresponding author: Xichuan Liu.)*

The authors are with the College of Meteorology and Oceanography, National University of Defense Technology, Nanjing 211101, China (e-mail: xmh1995@foxmail.com; liuxc2012@hotmail.com; 10290702@qq.com; songkun_0521@foxmail.com; general_zh@sina.com; 2009gaotc@gmail.com).

Digital Object Identifier 10.1109/JSTARS.2020.3004375

in the application of OELs: 1) identification of rain and no-rain periods; and 2) determination of attenuation baseline. It is worth noting that the two issues also exist in the use of HMLs.

The first issue is essential for determining the attenuation baseline during rain period, and many relevant methods have been proposed. Rahimi *et al.* used the relations between two different signals from dual-frequency microwave link to address this issue [19]. Schleiss *et al.* introduced a statistic that is related to signal variation and achieved the identification based on a given threshold [20]. Binsheng *et al.* extracted signal features with different time scale to train long short-term (LSTM) neural network that was used to distinguish the two situations [21]. Barthes *et al.* also proposed an identification method based on multilayer perceptron [8].

The second issue is an important process for obtaining the attenuation caused by rainfall. As for this, Jonatan *et al.* presented that minimal value of signal attenuation can be used for the determination of baseline [22]. Schleiss *et al.* introduced a moving time window to calculate attenuation caused by the factors other than rain [20]. Many researchers also suggested that the attenuation baseline during rain period can be obtained by interpolation according to the signal before and after rainfall [8], [12], [13]. However, if the rainfall lasts long time, the delay of rainfall measurements will become obvious.

With the development of machine learning, it is gradually being applied to precipitation observation [23]–[27]. To the best our knowledge, the earliest application of artificial neural network (ANN) to rainfall estimation can be traced back to 1992 when French *et al.* used current data to forecast rainfall an hour later by back-propagation (BP) neural network [23]. Similar rainfall measurement method was tested in many regions by Ahuna *et al.* and showed reliable performances [26]. In addition, Michaelides *et al.* used the ANN to fill up missing rainfall data [24], and Lathifah *et al.* identified different precipitation categories based on classification and regression tree [27]. In our work, we also try to propose a new rainfall inversion approach based on the machine learning because it can accurately establish the mapping relation between rainfall and satellite signal without any assumptions.

The primary aim of this article is to improve the practical application of rainfall monitoring by OELs. In this article, we set up an antenna in Nanjing to receive 12.32-GHz signal from AsiaSat5 and test our approach by this earth-space link.

First, we extract 12 statistical features from link signal, which have obvious differences between rain and no-rain periods. Then, these features are used to train support vector machine (SVM) that focuses on the identification of the two states. Due to the imbalance of data type, adaptive synthetic sampling algorithm (ADSYN) is adopted to improve the accuracy of SVM classifier. Second, we use the LSTM network to determine the attenuation baseline because it is capable of solving time-sequence problem. This method only depends on the signal prior to current rain period, which avoids the delay in rainfall measurement. Finally, we try to inverse precipitation based on the BP network because the selected features are related to rain intensity. The GA is also used to optimize the connection weights of BP network, which avoids the latter getting trapped into local optimal and speeds up convergence.

We achieve the identification of rain and no-rain periods with higher accuracy and determine the attenuation baseline in real time. Moreover, the GA-BP model shows a good performance on rainfall inversion. Although we only use single link to carry out our approach, the proposed algorithm is also applicable to multilinks with different frequencies and polarizations.

II. Materials and Methods

A. Rain Attenuation of Earth-Space Link

When the earth-space link passes through rainfall region, the scattering and absorption of raindrops will cause satellite signal attenuation. According to the analysis by Sheng *et al.* [28], the near scattered field of raindrops is negligible. Therefore, the specific attenuation $\gamma_{\rm rain}$ [dB/km] for raindrops in unit volume can be considered as the linear sum of extinction effects from each particle

$$\overline{\gamma}_{\rm rain} = 10\lg e \int_0^\infty \frac{\pi D^2}{4} Q_{\rm ext}(D) N(D) dD \tag{1}$$

where D is the equivalent diameter of raindrop [mm], $Q_{\rm ext}$ (D) is the extinction efficiency that can be obtained from T-matrix, and $N(D)$ is the equivalent raindrop size distribution (DSD) along the link. In fact, it has been proven that the specific attenuation is related to rain intensity in power-law manner [29]. And existing studies on path-average rain intensity R [mm/h] inversion by OELs are almost based on the power-law model (PL)

$$\bar{\gamma}_{\rm rain} = \alpha \bar{R}^{\beta} \tag{2}$$

where $\overline{\gamma}_{\rm rain}$ is the path-average specific attenuation, and the coefficients α and β are related to frequency, polarization, temperature, and DSD. Combining the distance l_r [km] of earth-space link in rainfall region, the rain attenuation A_R [dB] is described as

$$A_R = \bar{\gamma}_{\rm rain} l_r. \tag{3}$$

B. No-Rain Attenuation of Earth-Space Link

Compared to HMLs, there are more complicated atmospheric conditions affecting the earth-space link, which makes it more difficult to separate rain attenuation from satellite signal [30]. In application of HMLs, the assumption, that the horizontal distribution of oxygen and water vapor is constant, is widely adopted to simplify the rainfall inversion. Due to gas content changing with height, this assumption may be no longer valid. Moreover, the liquid water in cloud also affects the Ku band signal [31]. The scintillation caused by turbulence makes the signal amplitude fluctuates rapidly and irregularly [32]. In addition to the effects from above sources, nonatmospheric factors also have an influence on earth-space link such as free-space propagation and orbit perturbations; but these effects are generally constant or regular [12].

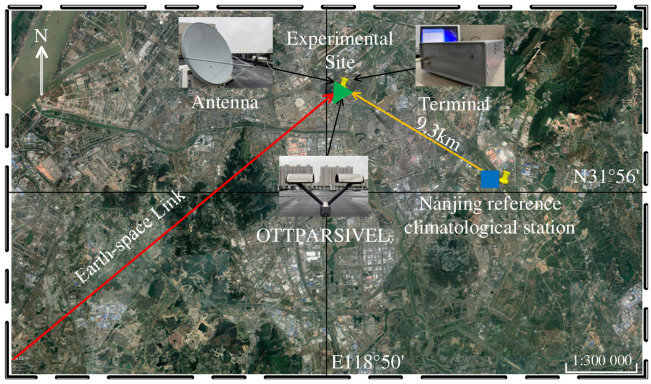

Fig. 1. Horizontal distribution of experimental site (green triangle) located in Jiangning district of Nanjing, China (31°58′27'N, 118°48′52'E), Nanjing reference climatological station (blue square) located about 9.8 km southeast of experimental site, and the earth-space link (red line). The antenna, OTTPARSIVEL (OTT) as well as terminal are located at the same position.

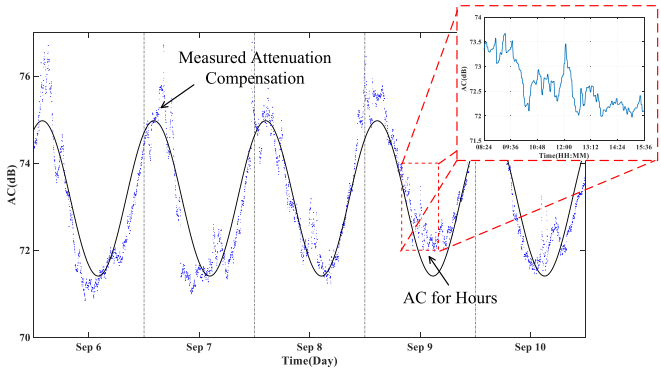

Fig. 2. When there is no rain, the obvious periodic variation of attenuation compensation (*AC*) due to obit perturbations is observed from measured values (blue dots), and by zooming into finer grade (red box) the fluctuations of amplitude are fast and irregular caused by atmospheric factors.

C. Experimental Setup

We establish the experimental system at Jiangning district of Nanjing, China (31°58'27'N, 118°48'52'E). A dish antenna in 1.2 m diameter receives vertically polarized signal in 12.32 GHz from AsiaSat5. This satellite operates in GEO above 100.5°E and emits relatively stable signal in C and Ku bands toward east Asia. The original received signal is transmitted to terminal and then the latter outputs processed signal once every 6 s for 24 h a day. In addition, an OTTPARSIVEL (OTT) is colocated with satellite antenna and provides rain intensity with 1-min temporal resolution. Radiosonde data from Nanjing reference climatological station is used to calculate the height of local rainfall region top. This station is located about 9.8 km southeast of our experimental site. The corresponding horizontal distribution of experimental system and climatological station is shown in Fig. 1. Furthermore, this experiment lasts three months from July to September 2019, and the measurements over this period are used to achieve the proposed approach.

The received signal power (P_r in dB) is described as (4), where P_e is the power of the satellite transmitter; G_e and G_r are the transmitter and receiver antennas gain; A_L is the free space attenuation, and A_t is the tropospheric attenuation [8]. Due to adopting an efficient hydrophobic coating, the wet antenna attenuation caused by residual water is negligible and thus not considered in this article

$$P_r(t) = P_e(t) + G_e(t) + G_r(t) - A_L(t) - A_t(t). \quad (4)$$

In the Ku band, A_t consists of attenuation caused by oxygen A_o, water vapor A_v, liquid water in cloud A_c, scintillation A_s, rain A_R, and other factors A_{other}, which is expressed by

$$A_t(t) = A_o(t) + A_v(t) + A_c(t) + A_s(t) + A_R(t) + A_{\text{other}}(t). \quad (5)$$

The processed signal from our terminal is defined as an attenuation compensation (*AC*, in dB) that is related to the gain provided by the receiver in order to compensate for the atmospheric attenuation. The relation between *AC* and A_t is

$$AC(t) = A_t(t) + C \quad (6)$$

where *C* is a constant.

To obtain the rain attenuation, (6) is described as

$$AC(t) = AC_{\text{base}}(t) + A_R(t) \quad (7)$$

where AC_{base} is the attenuation baseline denoted as

$$AC_{\text{base}}(t) = A_O(t) + A_V(t) + A_C(t) + A_S(t) + A_{\text{other}} + C. \quad (8)$$

During no-rain period, we have

$$AC_{\text{base}}(t) = AC_{\text{no-rain}}(t). \quad (9)$$

Fig. 2 shows the measured *AC* on five no-rain days from September 6 to 10. We can clearly observe the periodic variations of *AC* due to satellite perturbations (blue dots and black line). By zooming into finer grade (red box), the fluctuations of amplitude are very fast and irregular caused by turbulence and other atmospheric factors.

Although there are so many no-rain factors attenuating Ku band signal, rain is still the dominant factor in overall attenuation. It can be observed from the measurements (see Fig. 3) that the amplitude fluctuation of *AC* is obviously consistent with rain intensity. During rain period, *AC* is significantly higher than that of no-rain period, and the correlation coefficient between *AC* (red line) and rain intensity (blue line) is 0.78. Moreover, the green dotted line denotes the attenuation baseline in rain situation, which is used to obtain rain attenuation.

III. Earth-Space Link Rainfall Inversion Model

A. Identification of Rain and No-Rain Periods

In practice, the identification of rain and no-rain periods is a two-class classification problem: judge if it is raining at a given time. In present studies, many algorithms are designed to solve this problem such as probabilistic neural network, random forest (RF), and SVM, etc. The SVM is initially proposed to carry out two-class classification [33]. The theory of SVM is searching for

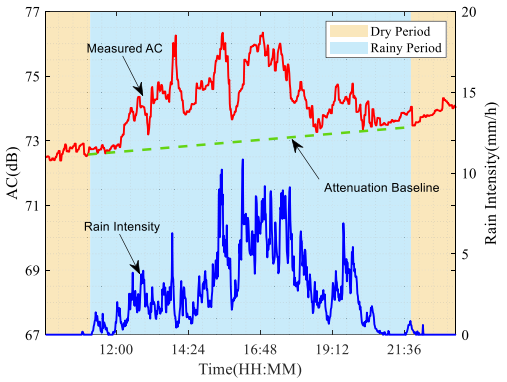

Fig. 3. This rain event happened on July 12, 2019. During rain period, the correlation coefficient between *AC* (red line) and rain intensity (blue line) is 0.78, and the green dotted line denotes the attenuation baseline.

an optimal hyperplane that separates the data into two classes. Its main objective in training process is to solve the following quadratic optimization problem [33]:

$$\min_{\alpha} \frac{1}{2}\sum_{i=1}^{n}\sum_{j=1}^{n}\alpha_i\alpha_j y_i y_j K\left(\mathbf{X}_i,\mathbf{X}_j\right)-\sum_{i=1}^{n}\alpha_i$$
$$\text{s.t.}\begin{cases}\sum_{i=1}^{n}\alpha_i y_i=0\\ 0\le\alpha_i\le C, i=1,2,\ldots,n\end{cases} \tag{10}$$

where $\mathbf{X}_i$ is the signal feature vector at the *i*th moment; $K(\mathbf{X}_i,\mathbf{X}_j)$ is the Gaussian kernel function used to change the dimension of sample space; *C* is the penalty coefficient; y_i is the corresponding label at the *i*th moment which can be described as

$$y_i=\begin{cases}0 \text{ if } R_{\mathrm{OTT}}\le 0.1 \text{ mm/h the } i\text{th moment } \in \text{ dry period}\\ 1 \text{ if } R_{\mathrm{OTT}}> 0.1 \text{ mm/h the } i\text{th moment } \in \text{ rain period}\end{cases} \tag{11}$$

where R_{OTT} is the rain intensity measured by OTT. Furthermore, the sequential minimal optimization algorithm is deployed in the SVM classifier training process.

According to the similar methods proposed by Barthes *et al.* [8] and Binsheng *et al.* [21], various characteristics with different time windows have been used such as standard deviation, local trend, and information entropy, etc. Based on these studies, we extract 12 statistical features from satellite signal to form the feature vector $\mathbf{X}_i$, which could discriminate between rainy and dry periods. Due to the limitation of OTT, the temporal resolution of selected feature is changed to 1 min. The time window of each feature should have a suitable length, because it relates to the time delay of rainfall measurement and meanwhile determines the feature differences between rain and no-rain. The 12 elements of $\mathbf{X}$ and corresponding symbols are tabulated in Table I.

The expression of the signal feature vector $\mathbf{X}_i$ is shown as follows:

$$\mathbf{X}_i=\left[x_1^i;x_2^i;x_3^i;\cdots;x_{11}^i;x_{12}^i\right]$$

TABLE I
STATISTICAL FEATURES OF EARTH-SPACE LINK SIGNAL WITH DIFFERENT TIME WINDOWS

Element	Feature	Time Window	Symbol
$x_1{}^i$	Standard Deviation	30min before *i*th moment	*std*
$x_2{}^i$	Local Trend	1min centered on *i*th moment	*trd*
$x_3{}^i$	Maximum	5min before *i*th moment	*max*
$x_4{}^i$	Minimum	5min before *i*th moment	*min*
$x_5{}^i$	Average	1min centered on *i*th moment	*ave*
$x_6{}^i$	Kurtosis	4min before *i*th moment	*kur*
$x_7{}^i$	Skewness	5min before *i*th moment	*ske*
$x_8{}^i$	Information Entropy	30min before *i*th moment	*en*
$x_9{}^i$	Ratio of Singular Values	30min before *i*th moment	*rsvd*
$x_{10}{}^i$	Ratio of High Frequency Energy to Low	30min before *i*th moment	*H/L*
$x_{11}{}^i$	Probability higher than *std*	\	*stdp*
$x_{12}{}^i$	Probability higher than *ave*	\	*avep*

$$\text{s.t.}\begin{cases}x_1^i=\left[\frac{1}{T+1}\sum_{t=1}^{T}\left(AC(i-T+t)-\overline{AC}\right)^2\right];\\ x_2^i=\frac{1}{T}\sum_{t=-T/2}^{-T/2}\alpha_t AC(i+t)\\ \alpha=(-1,-1,\ldots,-1,0,1,\ldots,1);\\ x_3^i=\text{maximum}(AC(i-T+t));x_4^i\\ \quad=\text{minimum}(AC(i-T+t));\\ x_5^i=\frac{1}{T}\sum_{t=1}^{T}AC(i-T+t);\\ x_6^i=\frac{T(T+1)}{(T-1)(T-2)(T-3)}\sum_{i=1}^{N}\left(\frac{AC(i-T+t)-\overline{AC}}{std(AC)}\right)^4\\ \quad-\frac{3(T-1)^2}{(T-2)(T-3)};\\ x_7^i=\left(\frac{1}{T}\sum_{t=1}^{T}\left(AC(i-T+t)-\overline{AC}\right)^3\right)\Big/\\ \quad\left(\frac{1}{T}\sum_{t=1}^{T}\left(AC(i-T+t)-\overline{AC}\right)^2\right)^{\frac{3}{2}};\\ x_8^i=\sum_{t=1}^{T}-AC_t\log(AC_t);\ x_9^i=\sum_{t=1}^{T/2}\lambda_t\Big/\lambda_1;\\ x_{10}^i=\sum_i\left[\omega_1(i)\right]^2\Big/\sum_{j=2}^{8}\sum_i\left[\omega_j(i)\right]^2;\\ x_{11}^i=P(\text{STD}>std_i);x_{12}^i=P(AVE>ave_i)\end{cases} \tag{12}$$

where *T* is the ratio of time window to the temporal resolution of *AC* equal to 6 s; ω_j is a coefficient sequence from satellite signal with three-layer wavelet decomposition; λ_t is the singular value of *Hankel* matrices composed by received *AC* over a 30 min time window; and the calculation of last two elements is based on the statistical database established by our experimental system. To diminish the effects caused by magnitude, it is necessary to normalize the feature so that their values fall into a specified range. In this article, we scale our features into the range [0,1]

TABLE II
VALUES OF MEAN AND STANDARD DEVIATION OF NORMALIZED FEATURES OF RAINY AND DRY MOMENTS

Features	\	*std*	*trd*	*max*	*min*	*ave*	*kur*	*ske*	*en*	*rsvd*	*H/L*	*stdp*	*avep*
Mean	**Rain**	0.111	0.504	0.345	0.322	0.331	0.504	0.062	0.666	0.330	0.081	0.854	0.770
	No-rain	0.029	0.563	0.194	0.195	0.192	0.501	0.061	0.806	0.191	0.025	0.481	0.485
Standard Deviation	**Rain**	0.135	0.065	0.150	0.136	0.143	0.114	0.128	0.141	0.140	0.094	0.187	0.241
	No-Rain	0.029	0.052	0.123	0.120	0.122	0.116	0.129	0.125	0.123	0.021	0.281	0.284

based on the following equation [34]:

$$\mathbf{V} = [v_1, v_2, \ldots, v_{12}] = \frac{(x_i - x_{i,\min})}{(x_{\max} - x_{\min})} i = 1, 2, \ldots, 12 \tag{13}$$

where $x_{i,\min}$ and $x_{i,\max}$ are the minimum and maximum values of each feature, respectively. The means and standard deviations of each normalized feature during rainy and dry periods are given in Table II. It shows that except the Kurtosis and Skewness, the means for each feature at rain and no-rain moments have obvious differences especially for the last two. The values of standard deviation in the two situations are very close except the first feature, indicating each of them has similar divergence.

In addition, the statistical distributions of each normalized features during rainy and dry periods are compared to test their ability to distinguish the two states. As can be seen in Fig. 4, the statistical distributions of characteristics at rain and no-rain moments are significantly different except Kurtosis and Skewness. As for the two features, their distributions at the two states are almost coincided with each other. However, in the training process, we found Kurtosis and Skewness enhanced the identification of some rain moments (highlighted by purple dotted line in figure), which is capable of improving the accuracy of the SVM classifier.

The correlation coefficients among extracted features and rain intensity are shown in Fig. 5. As can be observed, seven of these features, such as *trd*, *max*, *min*, etc., are highly correlated whose correlations are around 0.85. It also indicates that the rain intensity is related to these characteristics. The correlation with *H/L* is as high as 0.46, and values with other features are between 0.01 and 0.25.

B. Determination of Attenuation Baseline

Based on , attenuation baseline during rainy period is equal to the *AC* value measured by the satellite signal receiving system while no rain is observed by the OTT. Referring to the relevant literatures, the baseline can be estimated according to the values prior to this rain period, which actually is a time-series prediction problem [20], [22]. In fact, many methods are proposed to solve this problem such as Kalman Filter, generalized regression network, and least square method (LS), etc. In this article, we present a novel approach to predict attenuation baseline based on LSTM network that is a type of recurrent neural networks and first introduced by Hchreiter *et al.* [35]. The LSTM network is capable of learning long-term dependencies between time sequence data. The estimation of attenuation baseline only depends on the *AC* values before precipitation. Compared to the algorithm proposed by Barthes [8], the LSTM effectively avoids the time delay in rainfall measurement.

As can be seen from the left side of equation in Fig. 6, the LSTM block estimates $AC_{\text{base}}(t+1)$ based on the measured $AC_{\text{base}}(t)$ and its own outputs at t moment. The specific work process is explained on the right side in the chronological order. During dry period (yellow dotted box), the LSTM block receives the measured AC_{base}, equal to $AC_{\text{no-rain}}$, and previous information to adjust network parameters and predicts the AC_{base} for the next moment. During rainy period (blue dotted box), only previous information enters into the LSTM block to update network and meanwhile estimate AC_{base}. Generally speaking, the LSTM network learns the characteristics of measured AC_{base} at no-rain state in chronological order and then predicts the AC_{base} in rain situation, which belongs to supervised learning.

In the LSTM block, there are three gates: forget gate, update gate, and output gate. In work process, forget gate determines which part of the prior state $c(t-1)$ should be removed according to the information $h(t-1)$ from prior moment and the measured $AC_{\text{base}}(t)$. During rain period, this gate only considers the information $h(t–1)$. Update gate determines which information should be added to new state $c(t)$ according to its received data. On the basis of the first two gates, the output gate generates new state $c(t)$ and new information $h(t)$. At the same time, the estimated $AC_{\text{base}}(t+1)$ is also given by output gate. The update of LSTM network parameters is iteratively carried out by the following equations [36]:

$$\begin{cases} f_t = \sigma\left(W_{xf} x_t + W_{hf} h_{t-1} + b_f\right) \\ g_t = \sigma\left(W_{xc} x_t + W_{hc} h_{t-1} + b_c\right) \\ i_t = \sigma\left(W_{xi} x_t + W_{hi} h_{t-1} + b_i\right) \\ c_t = f_t \otimes c_{t-1} + i_t \otimes g_t \\ h_t = o_t \otimes \tanh\left(c_t\right) \end{cases} \tag{14}$$

where W and b denote the weights and bias of three gates, x represents the measured AC_{base} that is removed in rain situation and $\sigma(.)$ is the standard logistics sigmoid function.

C. Inversion of Rainfall

Based on above analysis, there is a certain correlation between rain intensity and selected features. Therefore, we try to propose a new approach to discuss the feasibility of rainfall inversion by BP network, because BP is capable of quickly establishing the mapping relation between inputs and outputs without any assumption. On the other hand, this new method is also capable of being generalized to other regions. As a type of multilayer feed forward ANN, conventional BP network comprises input layer, hidden layers, and output layer, and adjacent layers are

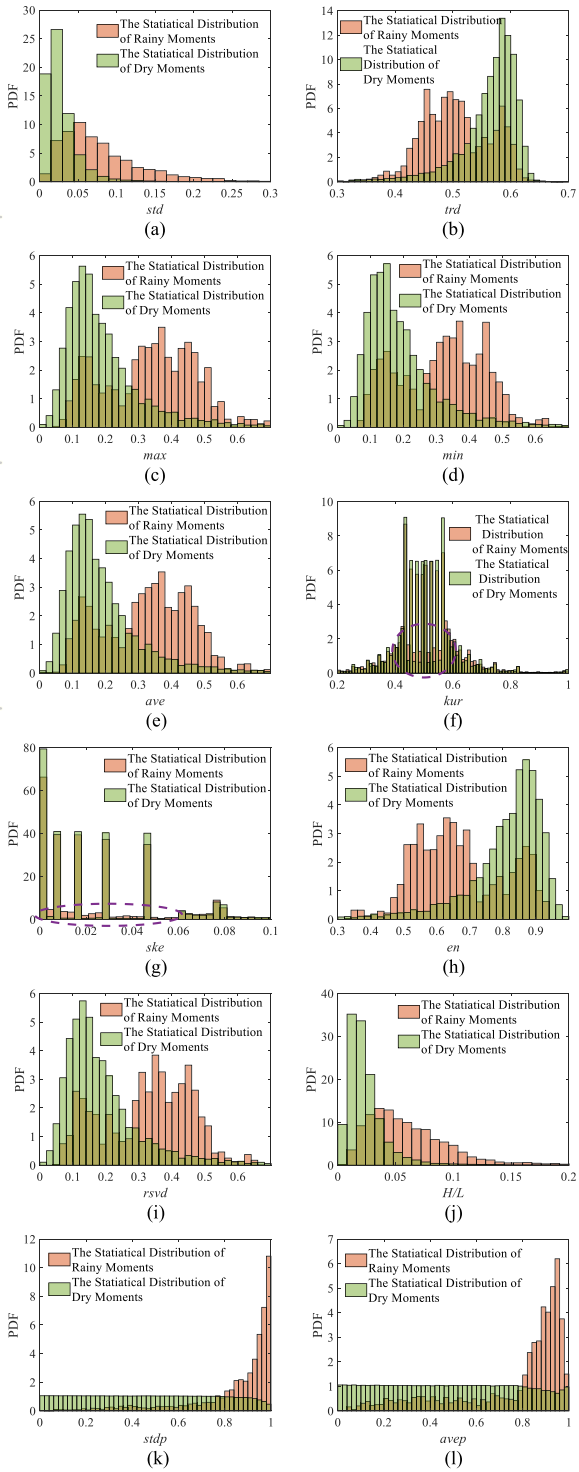

Fig. 4. Statistical distributions of normalized features in Table I are showed from (a) to (l) in order. Red and green bars are the distributions at rain and no-rain moments; the dark green bars are their overlapping parts; and the purple dotted lines highlight the differences between rainy and dry situations.

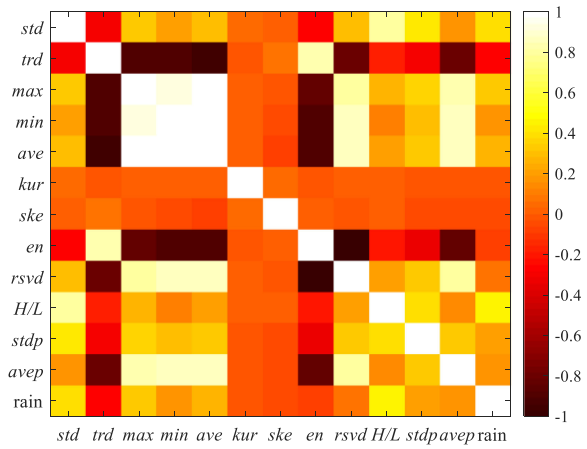

Fig. 5. Correlation coefficients among extracted features and rain intensity.

connected by corresponding weights [37], [38]. The network designed in this article consists of three hidden layers with 15 $\times$10 $\times$ 5 neurons. The input layer comprises 12 selected features as well as rain attenuation and the output is rain intensity.

The learning process of BP network can be divided into two steps: 1) forward propagation of feature signal and 2) back propagation of error signal. In the first step, the inputs are propagated to stimulate the first hidden layer's neurons. Then, the neurons of prior layer stimulate the next layer until generating estimated rain intensity. Note that in this process all connection weights remain unchanged. In the second step, according to the errors between estimations and measurements, BP network adjusts these weights along the direction of the fastest error gradient decent until the output is close to the expected one.

However, there are some inherent disadvantages with the conventional BP network such as poor rate of convergence and getting trapped into a local optimum easily [39], [40]. To overcome these drawbacks, many optimization algorithms have been introduced such as GA and particle swarm optimization algorithm. In this article, the GA is used to enhance the robustness and effectiveness of BP network. The training processes of GA-BP network are shown in Fig. 7. As can be seen, the GA actually optimize the generation of initial connection weights, which is important for the result of a BP network [38], [41]. In general, the optimization is carried out in the following way.

First, GA provides the initial weights that are close to global optimum. Based on this original state, BP network searches the optimal result in a small solution space. This method combines the advantages of these two algorithms. The GA as a heuristic stochastic search algorithm is good at searching global optimum and BP is more effective for the local search. The evolution process in GA mainly consists of selection, cross over, and mutation, which are performed for the individuals with high fitness. The specific calculation of GA can refer to the literature [41]. Moreover, the fitness used here is the reciprocal of test error E that is defined as

$$E = \frac{1}{2m} \sum_{i=1}^{m} (R_i - r_i)^2 \tag{15}$$

where m is the number of samples in test set and R and r are the measured and estimated rain intensity, respectively. The termination conditions are test error lower than 0.01 or procedure reaching maximum iteration that is set to 500.

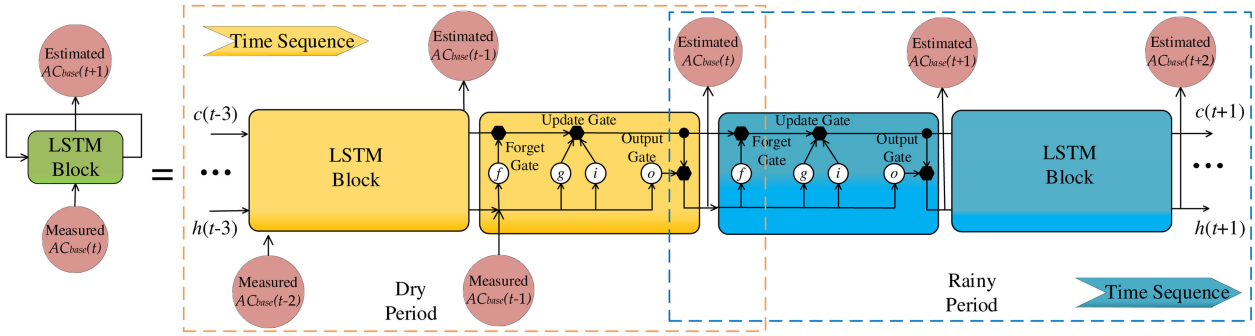

Fig. 6. Architecture of long short-term memory (LSTM) layer in this article. The yellow and blue dotted boxes indicate the working process of LSTM layer during no-rain and rain periods, respectively.

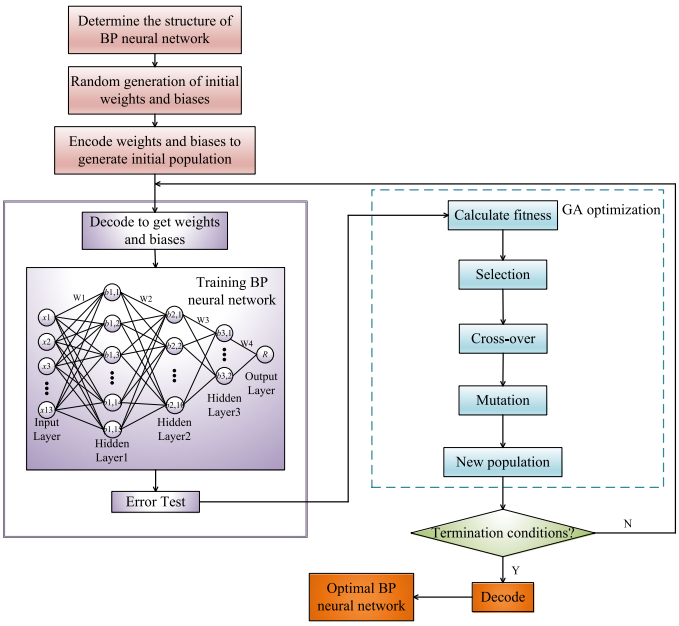

Fig. 7. Flowchart of GA-BP rainfall estimation model that consists of back propagation (BP) neural network module (the purple box) and genetic algorithm (GA) optimization module (the blue dotted box). The BP network comprises one input layer with 13 features, three hidden layers with 15×10×5 neurons, and one output layer with estimated rain intensity. In the GA optimization module, selection, cross over, and mutation are three basic operators to form new population.

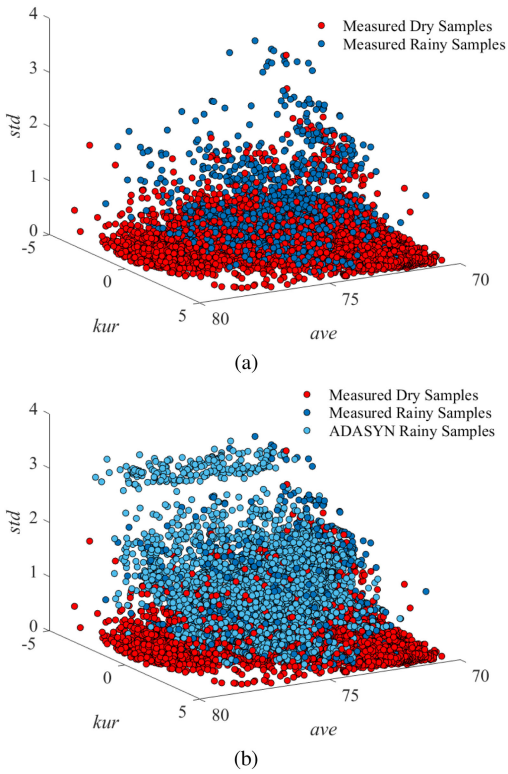

Fig. 8. Distribution of rainy and dry samples in the feature space before and after the ADSYN processing. (a) The original distribution (b) the distribution after processed by ADSYN.

IV. Results and Discussions

A. Validation of the SVM Classifier

Because the rain time in Nanjing is much less than the no-rain time, the ratio of rainy moments to dry is approximately equal to 1:20 [see Fig. 8(a)]. This situation makes the SVM classifier harder to learn the characteristics of minority class (rain), which has been exposed in the training process. The accuracy of rain-no-rain identification is lower than 40%. To diminish the effects caused by this problem, an oversampling approach, ADASYN, is used [42], [43]. This method is an improvement to synthetic minority oversampling technique. The ADSYN is capable of generating new minority samples around an original sample. The number of new produced samples depends on the distribution of learning weights that are related to the difficulty in learning original minority sample. The specific calculation process of ADSYN can refer to the literature [42]. After processed by the ADSYN, the ratio of rainy samples to dry raises to about 1:2 [see Fig. 8(b)].

Moreover, five evaluation metrics are used to assess the performance of the SVM classifier and they are defined as following equations [42]:

$$\begin{cases} \mathrm{OA} = \frac{\mathrm{TR}+\mathrm{TD}}{\mathrm{TR}+\mathrm{FR}+\mathrm{TD}+\mathrm{FD}} \\ \mathrm{Precision} = \frac{\mathrm{TR}}{\mathrm{TR}+\mathrm{FR}} \\ \mathrm{Recall} = \frac{\mathrm{TR}}{\mathrm{TR}+\mathrm{FD}} \\ F\_\mathrm{measure} = \frac{2\times\mathrm{Recall}\times\mathrm{Precision}}{\mathrm{Recall}+\mathrm{Precision}} \\ G\_\mathrm{mean} = \sqrt{\frac{\mathrm{TR}}{\mathrm{TR}+\mathrm{FD}}\times\frac{\mathrm{TD}}{\mathrm{TD}+\mathrm{FR}}} \end{cases} \tag{16}$$

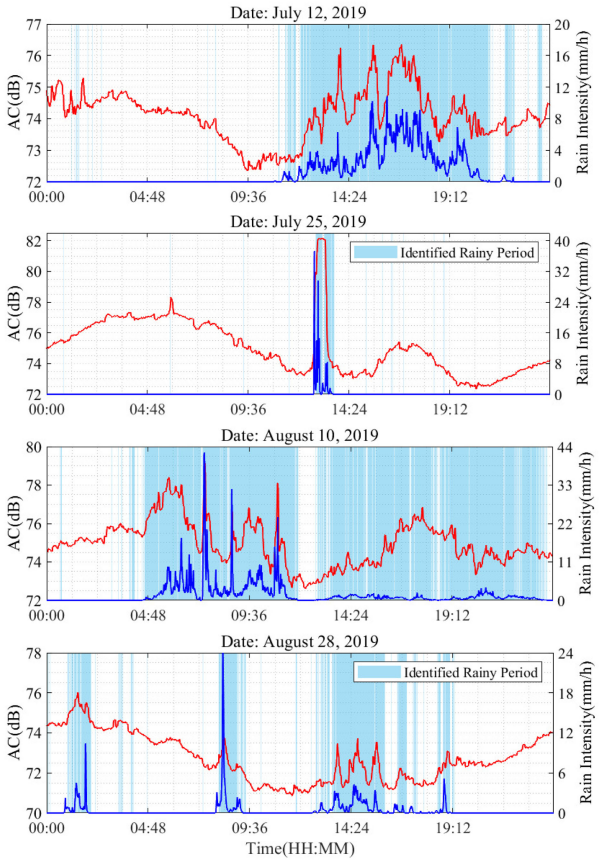

Fig. 9. Identification results of the SVM classifier on July 12, July 25, August 10, and August 28. The red line is *AC*, the blue line is rain intensity and the blue background denotes the rainy moments identified by SVM classifier.

where TR denotes the number of rainy samples that are identified correctly, TD denotes the number of dry samples that are identified correctly, FR is the number of no-rain samples that are identified as rain, and FD is the number of rain samples that are identified as no-rain. In addition, OA indicates the accuracy that the SVM classifier identify overall samples, *Precision* reflect the ability of classifier to distinguish the no-rain samples whose features are similar to that of rain, and *Recall* indicates the accuracy of identifying rain samples [44]. The aim of using ADSYN is to enhance the ability of SVM to identify rainy moment and meanwhile not reduce its performance on dry moment. Therefore, the *F_measure* combines *Precision* and *Recall* to assess the generalization of SVM to the two states. *G_mean* indicates the degree of inductive bias with respect to the accuracy of rain-no-rain identification [42]–[44].

The identification results on July 12, July 25, August 10, and August 28 are shown in Fig. 9. As can be seen, the SVM classifier has a good performance on different precipitation situations: continuous moderate rain (2.5–10 mm/h) on July 12, short-time heavy rain (10–50 mm/h) on July 25, continuous light rain (0–2.5 mm/h) on August 10 and intermittent light rain on August 28. However, many rainy moments are not identified accurately especially for the light rain, which can be observed from July 12 and August 28. This is because their corresponding signal features are very close to dry moment. It also can be seen on August 10, many dry moments appearing in rainy period are misidentified since signal features have no enough time to change back. On July 12, some dry moments are misclassified caused by the effects of other atmospheric factors.

Furthermore, Table III shows the statistical results of eight rainfall events. It can be seen on July 25 that the rainy moments of short-time heavy rain are identified easily; however, the *FR* is very close to the *TR,* which causes *Recall* is 1 but *Precision* is only 0.797. The values of *F_measure* on these events are all higher than 0.87 indicating the ability of the SVM classifier to identify rain and no-rain moments is close. Therefore, above results demonstrate that the method based on SVM achieves the rain-no-rain identification, but it is still insufficient for the recognition of light rain.

B. Attenuation Baseline From the LSTM Network

To evaluate the performance of LSTM network, estimated AC_{base} over 200 min after precipitation are used since the real baseline during rainy period cannot be obtained. The root-mean-square error (RMSE), coefficient of determination (R^2), and correlation coefficient (CC) are chosen as evaluation metrics and defined as follows:

$$\begin{cases} \text{RMSE} = \sqrt{\frac{1}{N}\sum_{i=1}^{N}\left(y_e(i)-y_r(i)\right)^2} \\ \text{R}^2 = 1-\sum_{i=1}^{N}\left(y_r(i)-y_e(i)\right)^2 \Big/ \sum_{i=1}^{N}\left(y_r(i)-\bar{y}_r\right)^2 \\ \text{CC} = \sum_{i=1}^{N}\left(y_e(i)-\bar{y}_e\right)\left(y_r(i)-\bar{y}_r\right) \Big/ \\ \quad \sqrt{\sum_{i=1}^{N}\left(y_e(i)-\bar{y}_e\right)^2}\sqrt{\sum_{i=1}^{N}\left(y_r(i)-\bar{y}_r\right)^2} \end{cases} \tag{17}$$

where y_e and y_r are the estimated and real values, respectively, and N is equal to 200.

The estimated attenuation baselines on July 6, July 9, July 19, and August 10 are shown in Fig. 10, where the picture at bottom left of each subgraph is the comparisons between measured and estimated AC_{base} in a finer grade and the bottom right is corresponding error. These results show the feasibility of the LSTM network to baseline prediction. Except for above days, Table IV also tabulates the evaluation metrics on other four precipitation days, which consist of different situations. In terms of RMSE and errors, the LSTM network has a good performance on predicting AC_{base} during rainy period. However, there are two obvious disadvantages that could be observed from R^2 and CC.

First, the rainfall characteristics of July 9 and July 19 are similar but their prediction results are obviously different. Based on lots of experiments, we found this problem often happens in the light rain that lasts a relatively long time because it makes other atmospheric factors such as water vapor change dramatically after the precipitation. However, this problem is not obvious in the continuous heavy rain (see August 10) since the effects caused by precipitation are more significant. Second, as can be seen from July 6, the value of R^2 is only 0.8. This is caused by short-time extreme rain (50 mm/h) whose effects are so significant that the signal has not yet changed back as entering dry period. This problem is particularly obvious in intermittent heavy or extreme precipitation. Based on the above

TABLE III
IDENTIFICATION RESULTS OF SVM CLASSIFIER ON EIGHT RAINFALL EVENTS

Date	*OA*	*Precision*	*Recall*	*F_measure*	*G_mean*	t_R	max_R
2019-7-06	0.993	0.930	0.952	0.941	0.974	55.85	4.40
2019-7-12	0.971	0.977	0.955	0.965	0.969	10.84	2.55
2019-7-13	0.984	0.954	0.930	0.942	0.961	4.82	0.31
2019-7-25	0.992	0.797	1.000	0.887	0.996	37.2	3.71
2019-8-10	0.950	0.994	0.939	0.966	0.961	42.27	3.78
2019-8-28	0.949	0.943	0.874	0.907	0.925	25.6	1.18
2019-9-02	0.955	0.992	0.855	0.918	0.923	6.05	1.20
2019-9-03	0.949	0.944	0.824	0.879	0.901	4.49	0.54

[a] t_R is the time of rainfall (in min) and max_R is the maximum of rain intensity.

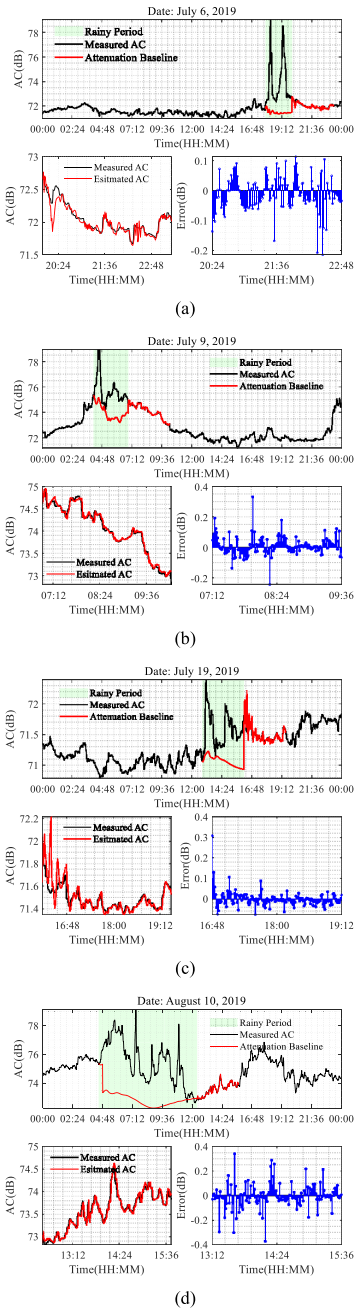

Fig. 10. Results of estimated attenuation baseline: (a) July 6, (b) July 9, (c) July 19, and (d) August 10. The picture at bottom left of each subgraph is the comparison between estimated and measured AC_{base} in a finer grade and bottom right is corresponding error. The red line is estimated attenuation baseline, the black line is measured *AC,* and the green background denotes the rainy period.

TABLE IV
EVALUATION METRICS ON ATTENUATION BASELINE PREDICTION OF EIGHT PRECIPITATION EVENTS

Date	RMSE	R^2	CC	t_R	max_R	ave_R
2019-7-06	0.097	0.804	0.914	126	55.85	4.40
2019-7-09	0.068	0.984	0.993	166	1.03	0.63
2019-7-13	0.078	0.990	0.995	400	4.82	0.31
2019-7-19	0.089	0.631	0.815	201	1.27	0.24
2019-8-04	0.049	0.900	0.952	51	25.15	3.39
2019-8-08	0.037	0.969	0.985	61	110.57	8.50
2019-8-10	0.090	0.952	0.976	476	42.27	3.78
2019-9-02	0.076	0.987	0.994	391	6.05	1.20

[a] ave_R is the average of rain intensity.

analysis, the LSTM network has a reliable performance on predicting attenuation baseline, but it still needs to be improved for overcoming the drawbacks occurring in the continuous light rain and intermittent extreme rain.

C. Rainfall Inversion by the GA-BP Model

As a comparison, the PL model is also used. Referring to ITU-R P.838, the coefficient α is equal to 0.027, and β is equal to 1.126 for 12.32 GHz [29]. The calculation of l_r is described as

$$l_r = h_r / \sin\theta \tag{18}$$

where θ is an antenna elevation angle and h_r is the height of rain region top. According to ITU-R P.839, the height can be obtained by [31]

$$h_r = h_0 + 0.36 \tag{19}$$

where h_0 is the height of 0 °C isotherm. We can obtain the statistical height of 0 °C isotherm in Nanjing from the appendix of ITU-R P.839, which is equal to 4.67 km [45].

However, in this article, the measured 0 °C isotherm height by radiosonde is used. Fig. 11 shows the values of 0 °C isotherm height from July to September, 2019, which is obviously different from the statistical value.

The comparisons of rain intensity and accumulated rain between OTT, PL, and GA-BP are given in Fig. 12. Here, only precipitation data are selected over three months and shown in the chronological order. As can be seen, estimations by GA-BP and PL models are consistent with OTT measurements. In terms of rain intensity, the RMSE, CC, and mean absolute deviation (MAD) of GA-BP model are 3.14 mm/h, 0.83, and 1.3 mm/h, which shows a better performance than the PL model whose values are 5 mm/h, 0.47 and 1.68 mm/h, respectively. In this

TABLE V
COMPARISONS BETWEEN OTT, GA-BP, AND PL ON TEN RAINFALL EVENTS

		OTT			GA-BP				PL			
Date	t_R	max_R	ave_R	ac_R	max_R	ave_R	ac_R	**RMSE**	max_R	ave_R	ac_R	**RMSE**
2019-7-06	126	55.85	4.40	555.0	22.02	5.45	686.9	7.38	9.96	3.24	407.8	8.19
2019-7-12	701	10.84	2.55	1788.1	8.30	2.11	1476.9	1.64	5.23	2.45	1714.1	1.64
2019-7-13	400	4.82	0.31	122.1	3.28	0.23	92.9	0.53	3.44	1.48	591.1	1.37
2019-7-25	61	37.20	3.71	226.5	23.49	5.95	362.7	6.60	9.81	5.17	315.1	7.38
2019-8-04	51	25.15	3.39	172.8	12.71	2.59	132.2	4.86	5.12	1.22	62.1	6.32
2019-8-08	61	110.57	8.50	518.5	84.99	8.74	533.4	9.13	9.38	1.79	109.0	21.74
2019-8-10	476	42.27	3.78	1798.9	23.11	3.65	1736.2	3.28	8.76	3.53	1680.6	4.26
2019-8-28	423	25.60	1.18	500.3	5.07	0.54	227.7	2.14	2.91	0.74	313.2	2.08
2019-9-02	391	6.05	1.20	468.1	4.40	1.04	405.1	0.84	3.98	1.96	767.7	1.10
2019-9-03	452	4.49	0.54	242.8	2.63	0.50	203.4	0.81	2.60	0.66	298.2	0.76

[a] ac_R is the total accumulated rain.

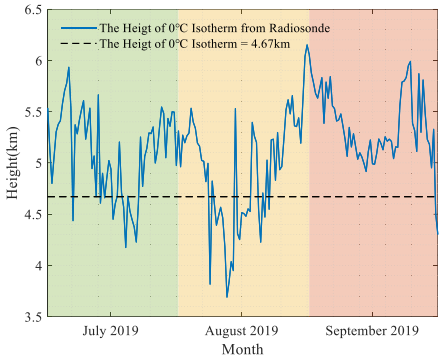

Fig. 11. 0 °C isotherm height from July to September, 2019 (blue line, measured by radiosonde) and the statistical height in Nanjing (black dotted line).

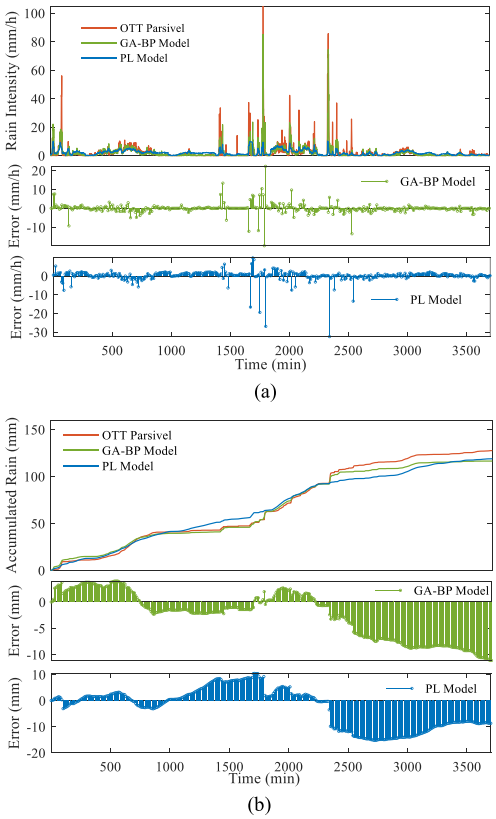

Fig. 12. Comparisons of rain intensity and accumulated rain between OTT, PL, and GA-BP over three months. (a) Rain intensity. (b) Accumulated rain.

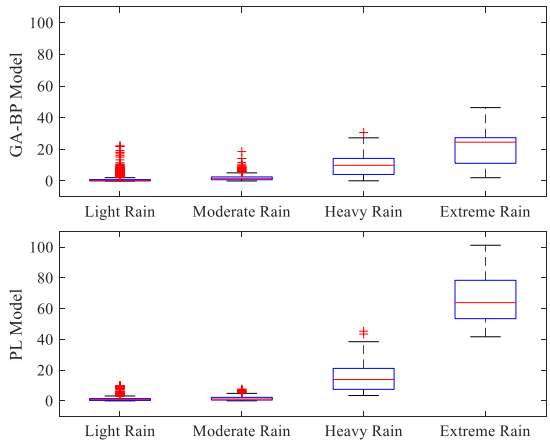

Fig. 13. Estimation errors of GA-BP and PL for different rainfall categories.

article, we use OTT measurements to train the GA-BP network and the rain-intensity provided by the PL model is actually path-averaged value, which accounts for the difference in rainfall inversion.

Moreover, ten rainfall events of various intensities and durations are selected. The dates, durations, measured, and estimated precipitation are given in Table V. It can be seen that the intensities given by OTT, GA-BP, and PL are close to each other especially for light (0–2.5 mm/h) and moderate (2.5–10 mm/h) rain events lasting long-time (events 2, 3, 9, and 10). However, for short-time heavy (10–50 mm/h) and extreme (50 mm/h) precipitation, the maximum values of rain intensity are obviously underestimated by GA-BP and PL (events 4, 5, and 6).

To evaluate the performances of GA-BP and PL on different precipitation categories, Fig. 13 shows the absolute error distributions between estimations and measurements. As also can be observed, the GA-BP and PL are good at light and moderate precipitation inversion whose error medians are close to zero. It can be seen that the width of the boxes and error increases with rain intensity. As for the GA-BP model, the samples of heavy and extreme precipitation in training set only accounts for 2.6% and 0.2% which causes the mapping relation between signal features and rain intensities are not obtained accurately. On the other hand, the presence of heavy and extreme rain often associates

with obvious spatial heterogeneity so that significant differences can appear because the measured volumes of atmosphere are different between the OTT and earth-space link. This explains the differences from the PL model since it provides the average rain intensity along link.

Compared with OTT measurements and PL estimations, the GA-BP model has a good performance on rainfall inversion, proving the feasibility of the proposed approach in this article. It also shows a great potential to use advanced machine learning algorithms for the precipitation monitoring by OELs.

V. Conclusion

Based on the exploitation of existing radio spectrum sources, the opportunistic use of widely distributed microwave links has a great potential for the global precipitation monitoring. This article improves the practical application of oblique earth-space links (OELs) to rainfall detection. A novel inversion method is proposed based on machine learning and capable of being generalized to other regions in the world.

In this article, we set up an antenna in Nanjing to receive 12.32-GHz signal from AsiaSat5. The data from satellite signal receiving system is used to achieve the proposed approach. First, 12 statistical features are extracted from the link signal and used to train SVM classifier that focuses on rain-no-rain periods identification. To diminish effects caused by the imbalance of data type, ADSYN is adopted. Second, the long-short term memory (LSTM) network is used to determine the attenuation baseline during rainy period because it is good at solving the time-sequence problem. During the experiment, we found the selected features are related to rain intensity so that the back propagation (BP) network is used to perform rainfall inversion. At the same time, we adopt the genetic algorithm (GA) to optimize the connection weights of BP, which avoids the latter getting trapped into local optimal and speeds up convergence. The main conclusions can be drawn from our work

1) For the identification of rainy and dry periods, the ADSYN effectively eliminates effects due to data imbalance, and the SVM classifier is capable of identifying the two states. The overall accuracy (*OA*) of identification is higher than 0.94 and the value of *recall* is higher than 0.82. However, the classifier is still insufficient for the recognition of light rain (0–2.5 mm/h) and easily disturbed by other atmospheric factors.
2) For the determination of attenuation baseline, we evaluate the performance of LSTM network based on the comparison between estimated and measured baseline over 200 min after precipitation, because the real value in rainy situation cannot be obtained. The RMSE is lower than 0.1 dB and CC is higher than 0.81 indicating a good performance of LSTM on the baseline determination. But it still needs to be improved for overcoming the drawbacks that occur in the continuous light rain (0–2.5 mm/h) and intermittent extreme rain (50 mm/h).
3) For the rainfall inversion, the comparisons of rain intensity and accumulated rain between OTT, GA-BP, and PL are performed. The estimations from GA-BP are consistent with OTT measurements whose RMSE and CC are 3.14 mm/h and 0.83, respectively. Moreover, the performances of GA-BP and PL on different precipitation categories are evaluated. Both methods are good at the inversion of light (0–2.5 mm/h) and moderate (2.5–10 mm/h) rain, but significantly underestimate heavy (10–50 mm/h) and extreme (50 mm/h) rain. In terms of GA-BP, this is because the samples of heavy and extreme rain in training set only account for 2.6% and 0.3%. On the other hand, the presence of heavy and extreme rain often associates with obvious spatial heterogeneity, which causes the differences between path-averaged (PL) and single-point measured (OTT) rain intensity. These results prove the feasibility of using machine learning algorithms to detect precipitation.

This article only uses single link to validate our approach, but the proposed method is also applicable to multilinks with different frequencies and polarizations. In the future, we will continue improving the performance of our approach in different regions and seasons. With the implementation of communication satellite constellation, using OELs for rainfall monitoring will become very common like water vapor measurement by global navigation satellite system. This work will also focus on the application of multilinks to regional rainfall monitoring and 3-D precipitation field reconstruction.

Acknowledgment

The author would like to thank the editor and anonymous reviewers for their valuable suggestions that improved our article. The data used in this study can be supplied via request to the corresponding author of this article.

References

[1] M. F. McCabe, "The future of earth observation in hydrology," *Hydrol Earth Syst. Sci.*, vol. 21, no. 7, pp. 3879–3914, 2017.
[2] H. Messer, A. Zinevich, and P. Alpert, "Environmental monitoring by wireless communication networks," *Science*, vol. 312, no. 1, p. 713, 2006.
[3] K. Song, T. Gao, X. Liu, M. Yin, and Y. Xue, "Method and experiment of rainfall intensity inversion using a microwave link based on support vector machine," *Acta Physica Sinica*, vol. 64, no. 24, pp. 1–8, 2015.
[4] T. Gao, K. Song, X. Liu, M. Yin, L. Liu, and S. Jiang, "Research on the method and experiment of path rainfall intensity inversion using a microwave link," *Acta Phsica Sinica*, vol. 64, no. 17, pp. 1–9, 2015.
[5] A. R. Rahimi, "Attenuation calibration of an X-band weather radar using a microwave link," *Amer. Meteorol. Soc.*, vol. 23, no. 3, pp. 395–405, 2006.
[6] S. Jiang, T. Gao, X. Liu, L. Liu, and Z. Liu, "Investigation of the inversion of rainfall field based on microwave links," *Acta Phsica Sinica*, vol. 62, no. 15, pp. 1–8, 2013.
[7] C. Han, J. Huo, Q. Gao, G. Su, and H. Wang, "Rainfall monitoring based on next-generation millimeter-wave backhaul technologies in a dense urban environment," *Remote Sens.*, vol. 12, no. 6, 2020, Art. no. 1045.
[8] L. Barthès and C. Mallet, "Rainfall measurement from the opportunistic use of an Earth–space link in the Ku band," *Atmos. Meas. Techn.*, vol. 6, no. 8, pp. 2181–2193, 2013.
[9] F. Mercier, L. Barthes, and C. Mallet, "Estimation of finescale rainfall fields using broadcast TV satellite links and a 4DVAR assimilation method," *J. Atmos. Oceanic Technol.*, vol. 32, no. 10, pp. 1709–1728, 2015.
[10] C. H. Arslan, K. Aydin, J. Urbina, and L. P. Dyrud, "Rainfall measurement using satellite downlink attenuation," in *Proc. IEEE Geosci. Remote Sens. Symp.*, Quebec City, QC, Canada, 2014, pp. 4111–4114.
[11] C. Mugnai, F. Cuccoli, and F. Sermi, "Rainfall estimation with a commercial tool for satellite internet in Ka band: Concept and preliminary data analysis," *Proc. SPIE*, vol. 9239, 2014, Art. no. 923904.

[12] F. Giannetti, M. Moretti, R. Reggiannini, and A. Vaccaro, "The NEFOCAST system for detection and estimation of rainfall fields by the opportunistic use of broadcast satellite signals," *IEEE Aerosp. Electron. Syst. Mag.*, vol. 34, no. 6, pp. 16–27, Jun. 2019.
[13] R. A. Giro, L. Luini, and C. G. Riva, "Rainfall estimation from tropospheric attenuation affecting satellite links," *Information*, vol. 11, no. 11, pp. 1–19, 2020.
[14] SpaceX, Mar. 20, 2018. STARLINK MISSION. [Online]. Available: https://www.spacex.com/webcast
[15] OneWeb, Mar. 31, 2020. OneWeb. [Online]. Available: https://www.oneweb.world/
[16] X. Shen, D. D. Huang, B. Song, C. Vincent, and R. Togneri, "3-D tomographic reconstruction of rain field using microwave signals from LEO satellites: Principle and simulation results," *IEEE Trans. Geosci. Remote Sens.*, vol. 57, no. 8, pp. 5434–5446, Aug. 2019.
[17] M. Xian, X. Liu, M. Yin, K. Song, and T. Gao, "Inversion of vertical rainfall field based on earth-space links," *Acta Physica Sinica*, vol. 69, no. 2, pp. 1–11, 2020.
[18] H. Messer, "Capitalizing on cellular technology—Opportunities and challenges for near ground weather monitoring," *Environments*, vol. 5, no. 7, 2018, Art. no. 73.
[19] A. R. Rahimi, A. R. Holt, G. J. G. Upton, and R. J. Cummings, "Use of dual-frequency microwave links for measuring path-averaged rainfall," *J. Geophys. Res.*, vol. 108, no. D15, pp. 1–12, 2003.
[20] M. Schleiss and A. Berne, "Identification of dry and rainy periods using telecommunication microwave links," *IEEE Geosci. Remote Sens. Letters*, vol. 7, no. 3, pp. 611–615, Jul. 2010.
[21] B. He, X. Liu, S. Hu, K. Song, and T. Gao, "Use of the C-band microwave link to distinguish between rainy and dry periods," *Adv. Meteorol.*, vol. 2019, 2019, Art. no. 3428786.
[22] O. Jonatan and M. Hagit, "Dynamic determination of the baseline level in microwave links for rain monitoring from minimum attenuation values," *IEEE J. Sel. Topics Appl. Earth Observ. Remote Sens.*, vol. 11, no. 1, pp. 24–33, Jan. 2018.
[23] M. N. French, W. F. Krajewski, and R. R. Cuykendall, "Rainfall forecasting in space and time using a neural network," *J. Hydrol.*, vol. 137, pp. 1–13, 1992.
[24] S. C. Michaelides, C. C. Neocleous, and C. N. Scguzas, "Artificial neural networks and multiple linear regression in estimating missing rainfall data," in *Proc. Int. Conf. Digital Signal Process.*, Limassol, Cyprus, 1995, pp. 668–673.
[25] M. N. Ahuna, T. J. Afullo, and A. A. Alonge, "Rainfall rate prediction based on artificial neural networks for rain fade mitigation over earth-satellite link," in *Proc. IEEE Africon*, Cape Town, South Africa, 2017, pp. 579–584.
[26] M. N. Ahuna, T. J. Afullo, and A. A. Alonge, "Rain attenuation prediction using artificial neural network for dynamic rain fade mitigation," *SAIEE Africa Res. J.*, vol. 110, no. 1, pp. 11–18, 2019.
[27] S. N. Lathifah, F. Nhita, A. Aditsania, and D. Saepudin, "Rainfall forecasting using the classification and regression tree (CART) algorithm and adaptive synthetic sampling (study case bandung regency)," in *Proc. 7th Int. Conf. Inf. Commun. Technol.*, Kuala Lumpur, Malaysia, Malaysia, 2019, pp. 1–5.
[28] P. Sheng, J. Mao, and J. Liu, *Atmospheic Pysics*. Beijing, China: Bejing Univ. Press, 2003.
[29] *Recommendation ITU-R P.838-3 Specific Attenuation Model for Rain for Use in Prediction Methods*, 2005.
[30] A. Dissanayake, J. Allnutt, and F. Haidara, "A prediction model that combines rain attenuation and other propagation impairments along Earth-satellite paths," *IEEE Trans. Antennas Propag.*, vol. 45, no. 10, pp. 1546–1588, Oct. 1997.
[31] *Recommendation ITU-R P.840 Attenuation Due to Clouds and Fog,* 2017.
[32] M. Singh, S. I. S. Hassan, M. F. Ain, and K. Igarashi, "Analysis of tropospheric scintillation intensity on earth to space in Malaysia," *Amer. J. Appl. Sci.*, vol. 3, no. 9, pp. 2029–2032, 2006.
[33] B. Scholkopf, J. C. Platt, J. Shawe-Taylor, A. J. Smola, and R. C. Williamson, "Estimating the support of a high-dimensional distribution," *Nerual Comput*., vol. 13, pp. 1443–1471, 2001.
[34] Mathworks, "Train support vector machine (SVM) classifier for one-class and binary classification," Mar. 20, 2020. [Online]. Available: https://ww2.mathworks.cn/help/stats/fitcsvm.html
[35] S. Hochreiter and J. Schmidhuber, "Long short-term memory(LSTM)," *Nerual Comput.*, vol. 9, pp. 1735–1780, 1997.
[36] Mathworks, "Long short-term memory networks," Mar. 14, 2020. [Online]. Available: https://ww2.mathworks.cn/help/deeplearning/ug/long-short-term-memory-networks.html
[37] J. Li, J. Cheng, J. Shi, and F. Huang, "Brief introduction of back propagation (BP) neural network algorithm and its improvement," *Ad. Comput. Sci. Inf. Eng.*, vol. 2012, pp. 553–558, 2012.
[38] D. Jahed Armaghani, M. Hasanipanah, A. Mahdiyar, M. Z. Abd Majid, H. Bakhshandeh Amnieh, and M. Tahir, "Airblast prediction through a hybrid genetic algorithm-ANN model," *Neural Comput. Appl.*, vol. 29, no. 9, pp. 619–629, 2016.
[39] S. Ding, C. Su, and J. Yu, "An optimizing BP neural network algorithm based on genetic algorithm," *Artif. Intell. Rev.*, vol. 36, no. 2, pp. 153–162, 2011.
[40] Y. Lee, S.-H. Oh, and M. W. Kim, "The effect of initial weights on premature saturation in back-propagation learning," in *Proc. IJCNN-91-Seattle Int. Joint Conf. Neural Netw.*, Seattle, WA, USA, USA, 1991, pp. 765–770.
[41] D. Gong, J. Sun, and Z. Miao, "A set-based genetic algorithm for interval many-objective optimization problems," *IEEE Trans. Evol. Comput.*, vol. 22, no. 1, pp. 47–60, Feb. 2018.
[42] H. He, Y. Bai, E. A. Garcia, and S. Li, "ADASYN Adaptive synthetic sampling approach for imbalanced learning," in *Proc. IEEE Int. Joint Conf. Neural Netw. World Congr. Comput. Intell.*, Hong Kong, China, 2008, pp. 1322–1328.
[43] B. Tang and H. He, "KernelADASYN Kernel based adaptive synthetic data generation for imbalanced learning," in *Proc. IEEE Congr. Evol. Comput.*, Sendai, Japan, 2015, pp. 664–671.
[44] H. He and E. A. Garcia, "Learning from Imbalanced data," *IEEE Trans. Knowl. Data Eng.*, vol. 21, no. 9, pp. 1263–1284, Sep. 2009.
[45] *Recommendation ITU-R P.839 Rain Height Model for Prediction Methods*, 2013.

Minghao Xian received the B.S. degree in atmospheric measurement techniques from National University of Defense Technology, Nanjing, China, in 2018, where he is currently working toward the M.S. degree in atmosphere science.

His research interests include atmospheric physics, atmospheric measurement, and remote sensing techniques and instruments.

Xichuan Liu received the M.S. degree in atmospheric measurement techniques and the Ph.D. degree in atmospheric measurement techniques both from PLA University of Science and Technology, Nanjing, China, in 2010 and 2014, respectively.

He is currently an Associate Professor with the College of Meteorology and Oceanography, National University of Defense Technology, Nanjing, China. His research interests include atmospheric physics, atmospheric measurement, and remote sensing techniques and instruments.

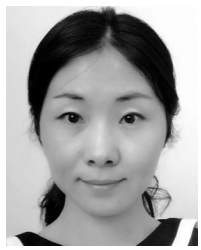

Min Yin received the M.S. degree in communication engineering and the Ph.D. degree in communication engineering both from PLA University of Science and Technology, Nanjing, China, in 2003 and 2006, respectively.

She is currently an Associate Professor with the College of Meteorology and Oceanography, National University of Defense Technology, Nanjing, China. Her research interests include atmospheric measurement by communication instruments.

Kun Song was born in China, in 1991. He received the B.S. and M. S. degrees in atmospheric measurement techniques from the PLA University of Science and Technology, Nanjing, China, in 2014 and 2017, respectively. He is currently working toward the Ph.D. degree in atmosphere science with National University of Defense Technology, Nanjing, China.

His research interests include atmospheric science, atmospheric measurement, and remote sensing techniques and instruments.

Shijun Zhao received the B.S. degree in atmospheric measurement techniques from the Air Force College of Meteorology, Nanjing, China, in 1999 and the M.S. degree in atmospheric physics from the PLA University of Science and Technology, Nanjing, China, in 2002.

He is an Associate Professor with the College of Meteorology and Oceanography, National University of Defense Technology, Nanjing, China. His research interests include atmospheric measurement and remote sensing techniques and instruments.

Taichang Gao received the B.S. degree in dynamic meteorology from the Air Force College of Meteorology, Nanjing, China, in 1982.

He is currently a Professor with the College of Meteorology and Oceanography, National University of Defense Technology, Nanjing, China. His research interests include atmospheric measurement and remote sensing techniques and instruments.